ADVANCED OPTICAL MATERIALS
www.advopticalmat.de

Strong and Broadband Pure Optical Activity in 3D Printed THz Chiral Metamaterials

Ioannis Katsantonis, Maria Manousidaki, Anastasios D. Koulouklidis, Christina Daskalaki, Ioannis Spanos, Constantinos Kerantzopoulos, Anna C. Tasolamprou, Costas M. Soukoulis, Eleftherios N. Economou, Stelios Tzortzakis, Maria Farsari,* and Maria Kafesaki**

Optical activity (polarization rotation of light) is one of the most desired features of chiral media, as it is important for many polarization-related applications. However, in the THz region, chiral media with strong optical activity are not available in nature. Here, a chiral metamaterial (CMM) structure composed of pairs of vertical U-shape resonators of "twisted" arms is studied, and it is revealed that it demonstrates large pure optical activity (i.e., optical activity associated with negligible transmitted wave ellipticity) in the low THz regime. The experimental data show polarization rotation up to 25° for an unmatched bandwidth of 1 THz (relative bandwidth 80%), from a 130 µm-thickness structure, while theoretical optimizations show that the rotation can reach 45°. The enhanced chiral response of the structure is analyzed through an equivalent RLC circuit model, which also provides simple optimization rules for the enhancement of its chiral response. The proposed chiral design allows for easy fabrication via direct laser writing (DLW) and electroless metal plating, making the associated structures suitable candidates for polarization control applications.

1. Introduction

Terahertz science is an active field of research both for its theoretical aspects but also due to the many associated applications,[1–6] especially in sensing, imaging, and future communications. The exploitation of THz waves in those applications, besides efficient sources and detectors, requires high-performance optical components, such as modulators, wave-plates, lenses, and so on. Hence, devices that can manipulate the amplitude and the phase of terahertz waves in an efficient and flexible way have gathered great attention.[7–9] Many innovating THz devices[10] and applications[11,12] require polarization control, such as polarization rotation. Proposed ways of realizing polarization rotators are based mainly on non-chiral anisotropic metasurfaces[13–15] or multilayer wire-grid polarizers oriented in different directions.[16,17] However, a crucial drawback of these approaches is that they work only for one polarization of the incident wave. In order to realize reciprocal polarization rotating devices insensitive to the polarization of the incident wave (at least for normal incidence) a chiral structure is necessary.[18–20] Chiral metamaterial structures, that is, metamaterials with unit-cells lacking any mirror-symmetry plane, have been shown in recent years able to give, among other effects, strong polarization rotation

I. Katsantonis, M. Manousidaki, A. D. Koulouklidis, C. Daskalaki, I. Spanos, C. Kerantzopoulos, A. C. Tasolamprou, C. M. Soukoulis, E. N. Economou, S. Tzortzakis, M. Farsari, M. Kafesaki
Institute of Electronic Structure and Laser
Foundation for Research and Technology-Hellas
Heraklion, Crete 70013, Greece
E-mail: katsantonis@iesl.forth.gr; mfarsari@iesl.forth.gr; kafesaki@iesl.forth.gr

The ORCID identification number(s) for the author(s) of this article can be found under https://doi.org/10.1002/adom.202300238

DOI: 10.1002/adom.202300238

I. Katsantonis, S. Tzortzakis, M. Farsari, M. Kafesaki
Department of Materials Science and Technology
University of Crete
Heraklion, Crete 70013, Greece

A. D. Koulouklidis, C. Kerantzopoulos, E. N. Economou
Department of Physics
University of Crete
Heraklion, Crete 70013, Greece

I. Spanos
Department of Engineering Science
University of Oxford
Oxford OX1 4BH, UK

A. C. Tasolamprou
Section of Electronic Physics and Systems
Department of Physics
National and Kapodistrian University of Athens
Athens 15784, Greece

C. M. Soukoulis
Ames Laboratory, U. S. Department of Energy and Department of Physics and Astronomy
Iowa State University
Ames, Iowa 50011, USA

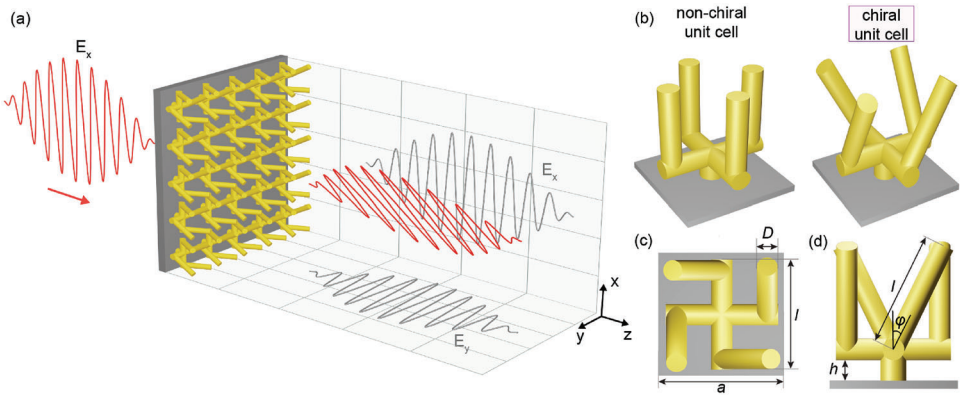

Figure 1. a) Illustration of our chiral metamaterial structure. Yellow color indicates the metallic components and light-gray the silicon substrate. b) Perspective view of our structure unit cell before (left panel) and after (right panel) the twist of the vertical arms. c) Top view of the chiral unit-cell and d) side-view of the unit-cell. The geometrical parameters are the following: Lattice constant $a = 120$ μm, arm length $l = 96$ μm (for both horizontal, i.e., at x–y plane and non-horizontal arms), arm diameter $D = 24$ μm, twist angle $\phi = 30^o$, vertical support-leg height $h = 18$ μm, and substrate thickness 1.5 μm.

(often called optical activity) even from ultrathin structures,[21–26] providing high efficiency which is limited only by dissipation loss and design optimization. We have to stress here that not only optical rotation but all the metamaterials-originated strong chiro-optical effects, for example, circular dichroism[24,27,28] and asymmetric transmission,[29–32] have been shown to be instrumental for many applications requiring wave polarization control,[21,33–35] including sensing[36–41] and spectroscopy.[42,43] These features may also be reconfigurable if combined with a THz tunable material like graphene.[44,45]

The key point in the metamaterial-based chiro-optical devices is that they exhibit chiro-optical effects orders of magnitude larger than natural chiral media; this is due to their macroscopic nature, where the currents responsible for chirality are not restricted by the atomic size. Furthermore, the scalability of metamaterials allows for operation in almost all frequency spectrum, provided that the available technology allows for their physical implementation. Indeed, chiral metamaterials based on bilayer-metal chiral meta-atoms,[24,26] such as pairs of crosses[46] or gamadions,[34] have demonstrated (with proper scaling) large optical activity in frequencies ranging from microwaves to the optical range. This type of chiral metamaterials supports multiple low-frequency resonant modes dominated by either an electric dipole resonant response or a magnetic dipole response, accompanied with chirality resonance; thus all chiro-optical effects are maximized at the resonances. Resonances though are associated also with high wave absorption and large impedance mismatch with the surrounding medium. Thus, the high optical rotation at resonance is always accompanied by low transmittance and by high circular-dichroism[21,47] (absorption difference between left-handed and right-handed circularly polarized waves), leading to unavoidable non-negligible ellipticity of the transmitted wave, an effect undesirable for many applications requiring linearly polarized waves. This high ellipticity of the bilayer metallic structures is boosted by the dielectric spacer separating the two metallic layers of the bilayer, where there is high electromagnetic field concentration and thus maximization of the absorption response. Thus, achievement of pure optical rotation (optical rotation associated with close to zero ellipticity) in bilayer-metal and in most of the resonant chiral structures seems possible only in frequency bands between resonances, with usually moderate rotation values and narrow-band response, features that inhibit the practical exploitation of the related structures.

Relatively recently, however, there have been demonstrated metamaterials able to realize significant pure optical rotation, own to particular meta-atom response, symmetries and couplings; various relevant meta-atoms have been proposed including multi-layer planar chiral designs,[26] 3D chiral structures,[48] and pseudo-planar metasurfaces.[49] Multi-layer chiral structures as in refs. [26, 50] demonstrated strong non-dispersive optical rotation in GHz frequency region with almost zero ellipticity. However, despite the non-dispersive optical activity, the relative bandwidth Δf is less than 50%, the transmittance is moderate in most of the high rotation band, and it is still challenging to fabricate the structure for use at higher frequencies. In the THz pseudo-planar metasurface of ref. [49], realized by 3D like gammadion shape meta-atoms, a strong optical activity was demonstrated accompanied though by strong ellipticity. Despite the remarkable efforts and interesting designs proposed so far, the achievement of broadband optical activity associated with negligible ellipticity and high transmittance still remains a challenging task, amenable to improvements.

In this work we aim to provide a significant contribution toward this direction. We propose a chiral metamaterial structure/design which shows large and ultra-broadband pure optical activity in the low THz regime. The structure is a metasurface made of 3D metallic elements; it is dielectrics-free and possesses fourfold rotational symmetry. The building block (meta-atom) is a pair of vertical U-shape resonators of "twisted" arms, as shown in **Figure 1**. This type of meta-atoms can be easily fabricated via direct laser writing (DLW)[51–54] and subsequent selective metallization by, for example, electroless plating. The geometry of our chiral design allows co-linear electric dipole and magnetic dipole moments (for normally-incident waves, i.e., along-z in Figure 1), resulting to bi-isotropic chiral response. We present an extensive theoretical and numerical analysis of the design and demonstrate its potential for strong and broad-band optical rotation accompanied with very low ellipticity. The numerical results are validated

by corresponding experimental data, validating also the large potential of our structure in the control of THz wave polarization.

The paper is organized as follows: Initially we present the proposed structure and demonstrate numerically its strong and broad-band pure optical activity response. Then, we describe the fabrication procedure and present the experimental results that validate the theory and reveal also experimentally the enhanced performance of the structure in terms of optical activity. Further, to explain the response of the structure, we employ a simple equivalent RLC circuit model for chiral metamaterials, which allows to derive simple optimization rules for achieving enhanced chiral response. In the conclusion, we summarize the main results and suggest future perspectives of this work.

2. Chiral Structure and Its Calculated Electromagnetic Response

A schematic representation of the chiral metamaterial (CMM) design proposed in the present study is illustrated in Figure 1. It consists of a square (in x–y plane) arrangement of chiral meta-atoms, where each meta-atom is formed by two perpendicular metallic U-shape rings of "twisted vertical" arms; that is, each initially vertical (to x–y plane—see Figure 1b) arm of the U-rings is rotated by an angle ϕ anti-clockwise (as seen from top—see Figure 1c), in respect to its initial U-plane. The twist (rotation) of the vertical arms induces a magnetoelectric coupling in the structure, resulting to the chiral response. In the absence of this twist (i.e., $\phi = 0$) the system behaves as typical non-chiral, split-ring-resonator-type metamaterial. The metal of the U-shape rings constituting the meta-atoms is Silver (Ag); its conductivity is considered in the simulations to be linearly dependent on frequency, ranging from $\sigma = 5.0 \times 10^7$ S m^{-1} at 0.1 THz to $\sigma = 0.86 \times 10^7$ S m^{-1} at 2.2 THz.[55–58] The structure stands on a silicon substrate (relative permittivity $\epsilon_{Si} = 11.9$ and loss tangent $\tan\delta = 0.02$; thickness in simulations 1.5 μm), while the short (of height $h = 18$ μm) vertical leg joining the rings with the substrate (it is electromagnetically inactive) serves the complete metal-plating of the horizontal U-arms in the fabricated structure. The lattice periodicity is $a = 120$ μm and the length of each arm is $l = 96$ μm. The arm diameter is $D = 24$ μm.

Scattering experiments/simulations provide a complete description of electromagnetic wave transmission and reflection by a structure. For chiral structures, where the eigenwaves are the circularly polarized waves, the scattering problem is usually formulated for circularly polarized light. However, there are many applications requiring linearly polarized waves while the experimental data taken, for example, from the spectrometers are usually obtained for linearly polarized electromagnetic fields. Having the reflection and transmission coefficients either for circularly or from linearly polarized waves one can calculate the main chirality related phenomena, that is optical activity and circular dichroism.

To demonstrate the broadband pure optical activity of our structure, we consider a unit cell as the one shown in Figure 1, with periodic boundary conditions along x and y directions, and calculate the transmitted fields for normally incident linearly polarized waves (using the commercial sofware package CST Studio as well as the commercial software COMSOL Multiphysics). In that case the incident (in) and transmitted (tr) electric fields ($\mathbf{E}$) are related via T_L matrix as

$$\begin{bmatrix} E_x^{(tr)} \\ E_y^{(tr)} \end{bmatrix} = \begin{bmatrix} t_{xx} & t_{xy} \\ t_{yx} & t_{yy} \end{bmatrix} \begin{bmatrix} E_x^{(in)} \\ E_y^{(in)} \end{bmatrix} = T_L \begin{bmatrix} E_x^{(in)} \\ E_y^{(in)} \end{bmatrix} \quad (1)$$

In Equation (1) t_{xx}, t_{yy}, t_{xy}, and t_{yx} are the complex transmission coefficients, where the first subscript indicates the output wave polarization and the second the incident wave polarization. Due to the fourfold rotational symmetry of our structure $t_{xx} = t_{yy}$ and $t_{xy} = -t_{yx}$.

To evaluate the chiral response of our structure, we need to calculate the transmitted wave ellipticity, $\eta = 0.5\tan^{-1}[(|t_{++}|^2 - |t_{--}|^2)/(|t_{++}|^2 + |t_{--}|^2)]$, directly connected to the circular dichroism, $CD = |t_{++}|^2 - |t_{--}|^2$, as well as the polarization rotation angle, $\theta = (1/2)[\arg(t_{++}) - \arg(t_{--})]$, a measure of the optical activity. To obtain η and θ we need the corresponding transmission coefficients for right-handed and left-handed circularly polarized waves, t_{++} and t_{--} respectively; they can be obtained from the corresponding linear polarization coefficients using the general formula[29]

$$T_{CP} = \begin{bmatrix} t_{++} & t_{+-} \\ t_{-+} & t_{--} \end{bmatrix} = \frac{1}{2} \begin{bmatrix} (t_{xx} + t_{yy}) + i(t_{xy} - t_{yx}) & (t_{xx} - t_{yy}) - i(t_{xy} + t_{yx}) \\ (t_{xx} - t_{yy}) + i(t_{xy} + t_{yx}) & (t_{xx} + t_{yy}) - i(t_{xy} - t_{yx}) \end{bmatrix} \quad (2)$$

which is simplified in our case taking into account the symmetries $t_{xx} = t_{yy}$ and $t_{xy} = -t_{yx}$ (these symmetries result to $t_{+-} = t_{-+} = 0$).

The calculated co- and cross-polarized transmittances ($T_{xx} = |t_{xx}|^2$, $T_{yx} = |t_{yx}|^2$) as well as the corresponding optical rotation, θ, and ellipticity, η, for our structure are illustrated in **Figure 2**a–c. We observe two strong resonances, at 0.76 and 1.74 THz, associated with dips in co-polarized transmittance and peaks in the cross-polarized one. In the case of no-twisted U-arms ($\phi = 0$) both resonances are coming from the U-ring which is perpendicular to the incident magnetic field, as shown by field and current simulations. The first resonance is a typical magnetic resonance, excited both by the incident magnetic field and the incident electric field (the latter due to the bianisotropy of the ring,[59,60] coming from the asymmetry of the U-shape in the direction of the electric field). The second resonance is predominantly the electric dipole resonance of the parallel to the electric field U-ring; it is though strongly affected by the coupling between neighboring unit-cells (note that the "vertical" U-arms of neighboring cells form pairs of parallel cut-wires supporting also resonant magnetic response). The twisting of the U-arms ($\phi = 30^o$) results to excitation of both U-rings forming our meta-atom; for both rings co-linear electric and magnetic dipoles are excited, resulting to chiral response and thus to the resonant cross-polarized transmission shown in Figure 2a.

Using the transmission data for linearly polarized waves, we obtain the corresponding ones for cicrulary polarized waves (via Equation (2)) and through them we evaluate the optical activity and transmitted wave ellipticity for our structure. The corresponding results are shown in Figure 2b,c; they reveal a quite

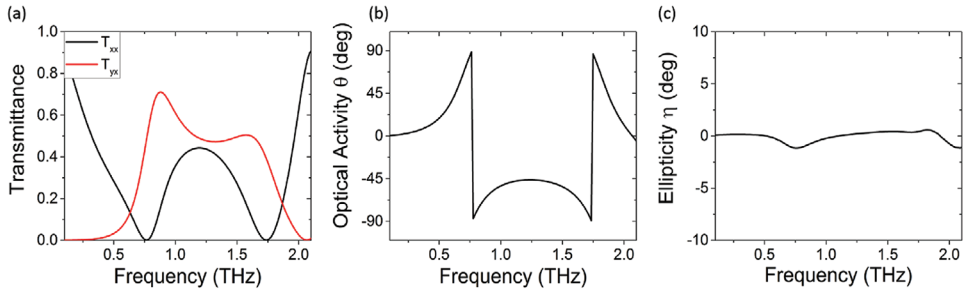

Figure 2. Panel (a) depicts the numerically calculated co- and cross-polarized transmittance spectra (black-line, T_{xx}, and red-line, T_{yx}, respectively) for the structure of Figure 1. Panels (b) and (c) illustrate the corresponding optical activity and ellipticity of the transmitted wave.

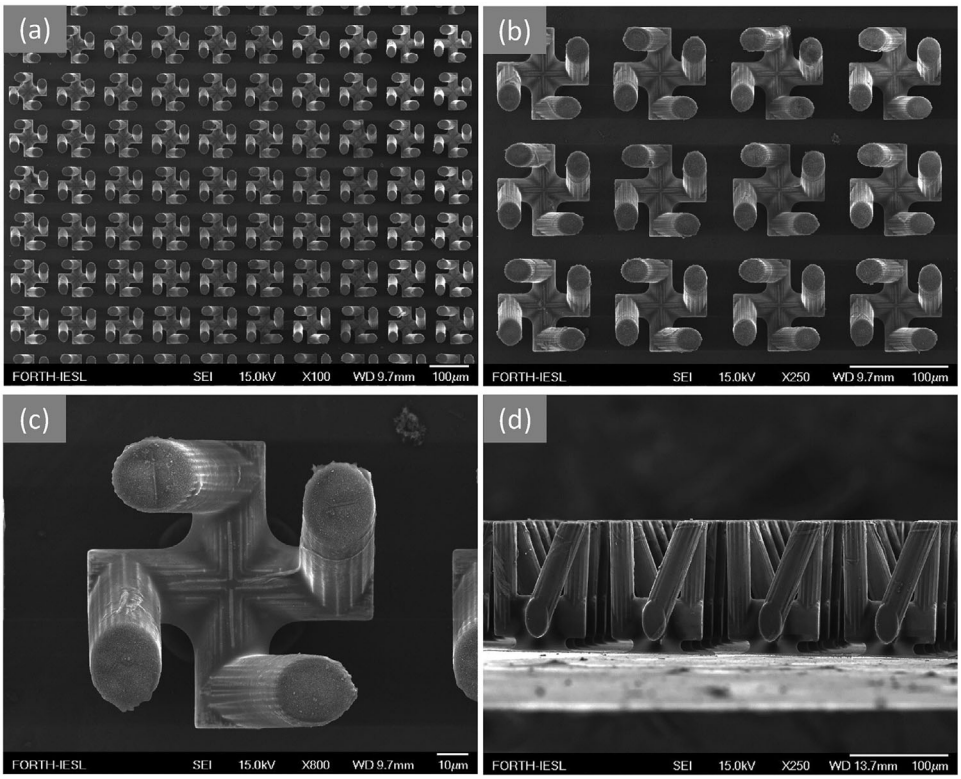

Figure 3. Scanning electron images (SEM) of the metalized Chiral THz metamaterial structures fabricated on a silicon substrate. a–c) Top view and d) side view. The geometrical dimensions of the structure are measured to be: lattice periodicity a = 121.4 μm, arm length l = 92.8 μm, arm diameter D = 24 μm and angle of the arm $\phi = 21°$.

impressive pure optical activity (i.e., optical activity associated with negligible ellipticty). The optical activity is larger than 45° in the range from 0.76 to 1.74 THz, that is, in a relative bandwidth $\Delta f \simeq 80\%$ ($\Delta f = 100 \times (f_{max} - f_{min})/(f_{max} + f_{min})/2$). The ellipticity in this range is always lower than 2°. This small ellipticity is attributed partially to the dielectrics-free nature of the structure.

Thus, we can summarize that for our proposed design, numerical simulations demonstrate large, pure and broadband optical rotation of linearly polarized waves. This enhanced performance will be verified by the associated experimental studies presented below, and will be discussed further and analyzed in Section 4.

3. Fabrication and Electromagnetic Characterization

In order to fabricate the metamaterial structure depicted in Figure 1, we employed direct laser writing (DLW) by multiphoton polymerization (MPP),[61,62] followed by selective metallization through electroless plating (EP) with silver.[63] The detailed experimental setup used for the fabrication and the subsequent metallization of the fabricated structures is presented at the Experimental Section of this paper. Scanning electron microscope images (SEM) of the fabricated metalized chiral THz metamaterial structures are shown in **Figure 3** in top and side view. The geometrical parameters of the metallic structures are measured to be

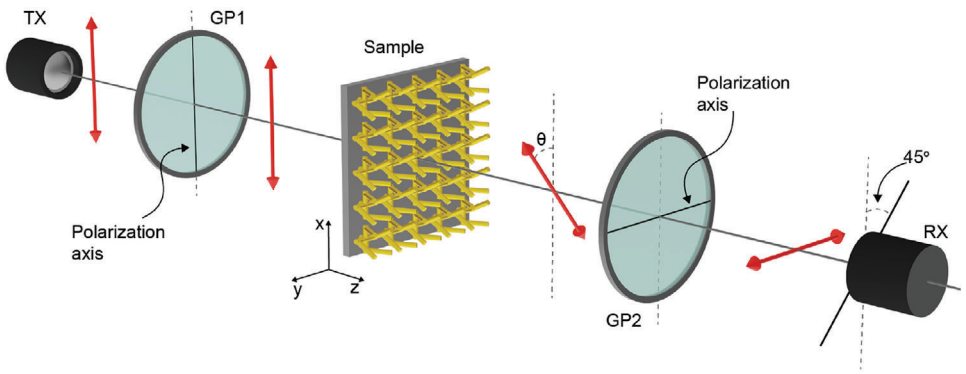

Figure 4. Schematic representation of the experimental setup. TX:THz emitter, GP1,2:Wire grid polarizers, RX: THz receiver, rotated at 45° with respect to *x*-axis.

the following: the lattice constant $a = 121.4$ μm, the arm length $l = 92.8$ μm, the arm diameter $D = 24$ μm, and the angle of the arm $\phi = 21°$ (note the deviations in the geometrical parameters from the optimized simulated structure of Figure 2). The structure is fabricated on a 530 μm thick silicon substrate.

To determine the optical characteristics of our chiral metamaterial, we used a terahertz time-domain spectroscopy (THz-TDS) setup based on photoconductive antennas (TOPTICA TeraFlash pro) operating in transmission mode. A schematic representation of the experimental setup in shown in **Figure 4**. A broadband THz pulse, linearly polarized along the *x*-axis, is generated by the photoconductive emitter (TX). The THz pulse passes through a wire grid polarizer (GP1) that further defines the polarization along the same axis and impinges on the sample at normal incidence. The transmitted by the sample wave, then, passes through a second wire grid polarizer (GP2) which can be either parallel or perpendicular to GP1. This way, cross- or co-polarized transmission measurements can be performed. The THz wave is finally guided to the photoconductive detector (RX). Since RX is highly sensitive to linearly polarized THz waves, it was rotated by 45° with respect to *x*-axis. This ensures that there is always an equal component of the THz field along the *x*- and *y*-axis.[64,65] The THz transmission spectra were normalized to a co-polarized transmission spectrum through a bare silicon substrate. Note that in the measurements, to eliminate the influence of the substrate Fabry–Perot resonances in the transmission, we record only the first part of the transmitted pulse, and not the secondary pulses, corresponding to multiply scattered waves. **Figure 5** shows the measured transmission power spectra ($T_{xx} = |t_{xx}|^2$ and $T_{yx} = |t_{yx}|^2$) of our metamaterial at linear polarization incidence, as well as the corresponding optical activity, θ, and ellipticity η.

To compare our experimental results to the numerical ones, the same calculations presented before are used. The corresponding data are shown also in Figure 5, next to the experimental ones. For the calculations we assume the following geometrical parameters which are the same as the fabricated sample (with a deviation less than 1%) with bulk Ag conductivity in the range from $\sigma = 8.7 \times 10^6$ S m^{-1} at 0.1 THz to $\sigma = 3.5 \times 10^6$ S m^{-1} at 2.2 THz as in ref. [63]. Particularly, the lattice constant is $a = 120$ μm, the arm length is $l = 90$ μm while each arm is rotated by an angle $\phi = 20°$, the arm diameter is $D = 24$ μm and the support vertical leg is $h = 18$ μm. The substrate thickness is considered also

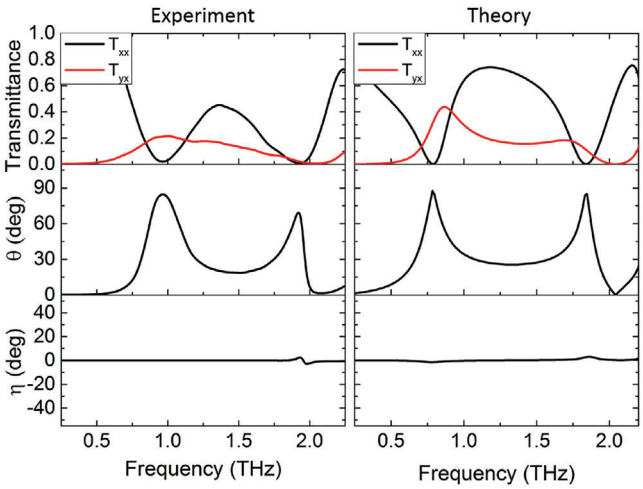

Figure 5. The three left-hand side panels show experimentally measured co- and cross- polarized transmittances (top left), optical activity, θ (middle left), and ellipticity, η (bottom left). The corresponding simulation results are illustrated in the right-panels and are in good agreement with the experimental data.

here very small (1.5 μm), as for the results to be directly comparable with the experimental ones where the influence of the subtrate Fabry–Perot resonances has been eliminated. (Note that systems composed of chiral metamaterials and a thicker Silicon substrate have more complex scattering response; sharp Fabry–Perot resonances appear[66] generated by interference of the forward/backward propagating waves in the substrate.)

In Figure 5, as expected, strong polarization rotation with almost zero ellipticity is obtained, for a bandwidth of 1 THz. The optical measurements of our fabricated sample represent this trend very nicely, as can be observed in the left column of Figure 5. In particular, the measured co-polarization transmission amplitude, T_{xx} in the spectra range from 1 to 2 THz is compressed below 50%. At the same time, the cross-polarization transmission amplitude, T_{yx}, reaches its maximum value of 20%, indicating effectively the polarization rotation of linearly polarized waves. Using the experimental data, we evaluate the polarization rotation angle and ellipticity as depicted in the left-hand side panels of Figure 5. We observe optical activity up to 25° for a

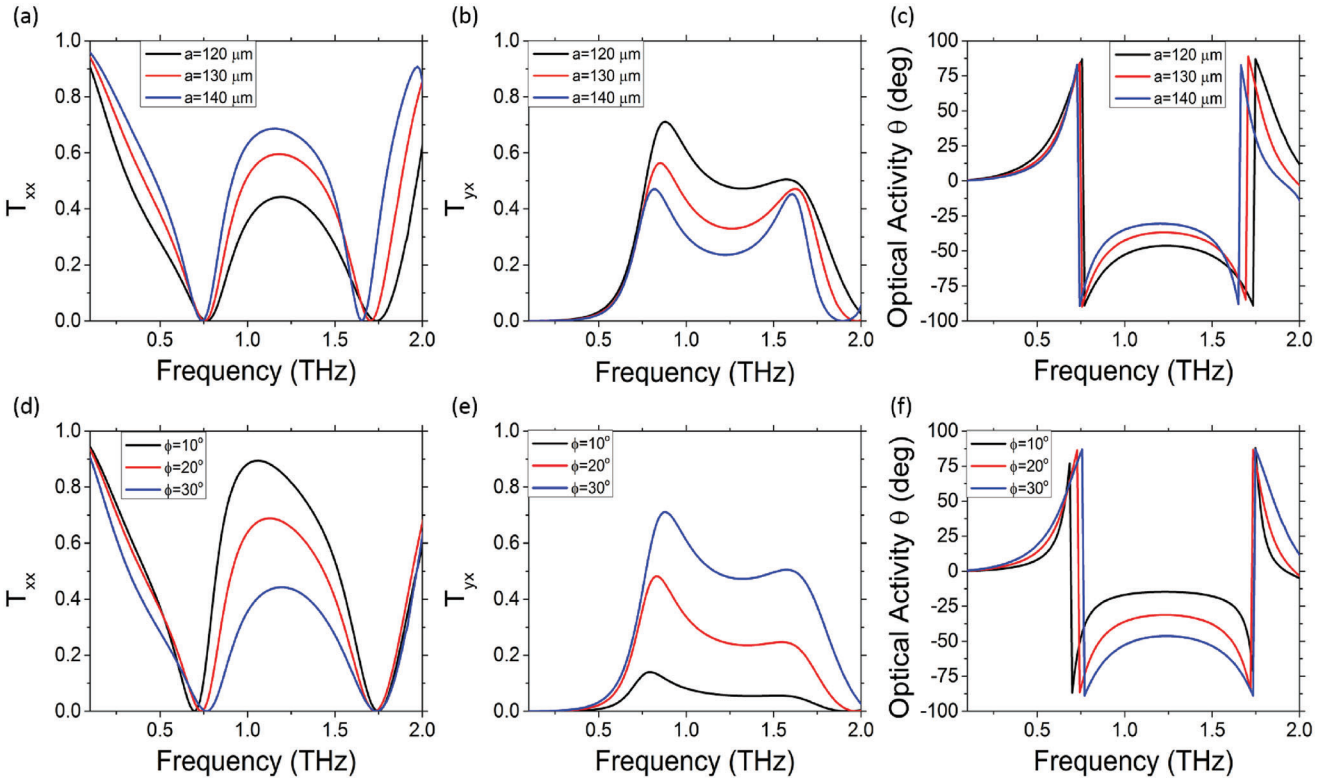

Figure 6. The top panels (a–c) depict the numerically calculated co- and cross- transmittance spectra and the corresponding optical activities at different lattice-constants (a) of our metamaterial. In the bottom panels (d–f), the numerically calculated co- and cross-polarized transmittance spectra and the corresponding optical activities at three different rotation angles of the U-rings arms: $\phi = 10°$, $\phi = 20°$, and $\phi = 30°$, of arms.

frequency range over 1 THz accompanied by zero ellipticity. However, the experimental curves are a bit lower than the theoretical ones, and the first resonance appears at somewhat higher frequency than expected from simulations. This difference can be attributed mainly to the difference in the conductivity of the Silver coated sample compared to the bulk conductivity used in the simulations as well as to fabrication imperfections, especially in the cross-sections of the cylindrical arms which are in some cases elliptical instead of circular. Furthermore, at low THz the skin-depth of Silver, strongly depends on the value of the conductivity,[67] and in some cases the skin depth can be larger than the achieved of the deposited metal.

4. Theoretical Analysis and Discussion

In this section we discuss first the sensitivity of the electromagnetic response of our design for different geometrical parameters. In particular, we demonstrate the effect of changing the in-plane lattice constant (affecting the coupling with the nearest neighbors) and the vertical arms rotation angle (ϕ) on the transmittance features as a function of frequency. The co- and cross- polarized transmittances ($T_{xx} = |t_{xx}|^2$, $T_{yx} = |t_{yx}|^2$) for different lattice-constant values, a, (keeping the vertical arms rotation angle, $\phi = 30°$, constant) as well as the corresponding optical rotations, θ, are illustrated in **Figure 6**a–c. We observe that the increase of the lattice constant leads to lower cross-polarized transmittance and optical rotation values. It does not affect strongly though the position of the resonances, indicating that the nearest-neighbor coupling is not a parameter determining or dominating the structure response.

Regarding the effect of the rotation angle, ϕ, it is demonstrated in Figure 6d–f. Since the system is non-chiral in the absence of rotation, $\phi = 0$, of the arms, we expect that by tuning the angle ϕ (keeping the lattice-constant $a = 120$ μm) we can highly control the optical activity. Indeed, the numerical data of Figure 6d,f verify this tunability potential, demonstrating once again the strong, broadband, and relatively flat pure optical activity of our structure. We have to note here that this response is maintained until $\phi = 45°$; above this value, the chiral response becomes more and more weak and for $\phi = 90°$ (gammadion shape) the optical activity becomes zero as expected due to the fact that a planar single gammadion meta-atom is achiral for normal incidence.

To understand and explain the calculated and measured response of our structure, we perform a theoretical analysis for obtaining qualitative formulas for the material parameters determining the structure response, and in particular for evaluating the effective chirality close to the first structure resonance.

We consider our meta-atom element consisting of two perpendicular U-shaped rings, as shown in **Figure 7**, and we examine the response of both rings to an incident EM field. Each U-ring is considered as a polarizable particle showing electric and magnetic dipole response; the electric and magnetic dipole

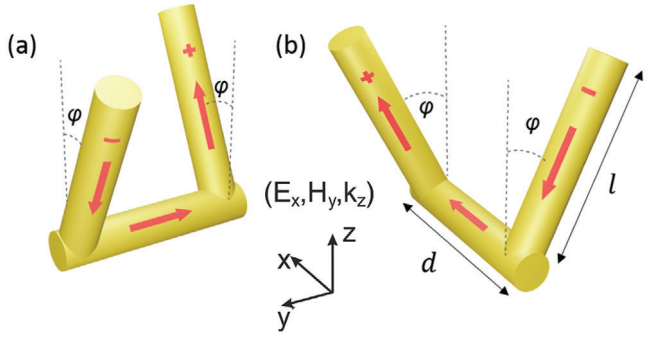

Figure 7. The two topologies, (a) and (b), of the basic chiral metallic element constituting the meta-atom of our structure (the meta-atom is the addition of the two topologies). Both topologies are the same U-shaped ring of twisted (by an angle ϕ) vertical arms. The components of the incident electromagnetic wave are also marked in the figure, along with the currents they excite (red arrows) in the frequencies around the first structure resonance (magnetic-type resonance).

moments, **p** and **m** respectively, are connected with the local fields by[18,68]

$$\mathbf{p} = \bar{\bar{\alpha}}_{ee}\mathbf{E} + \bar{\bar{\alpha}}_{em}\mathbf{H}, \qquad \mathbf{m} = \bar{\bar{\alpha}}_{mm}\mathbf{H} + \bar{\bar{\alpha}}_{me}\mathbf{E} \tag{3}$$

where $\bar{\bar{\alpha}}_{ee}$, $\bar{\bar{\alpha}}_{mm}$, $\bar{\bar{\alpha}}_{em}$, $\bar{\bar{\alpha}}_{me}$ are the electric, magnetic, electromagnetic, and magnetoelectric polarizability tensors of the U-ring and the **E**, **H** indicate the local fields (i.e. external fields plus fields generated by the induced currents at the ring; we omit for simplicity any coupling between unit cells, and we consider operation in the quasistatic limit).

Considering the incident field configuration shown in Figure 7, the induced currents at the lowest frequency resonance are as shown by the red arrows. Calculating the currents and/or the accumulated charges one can evaluate the electric and magnetic dipole moments relevant to each ring and through them the individual polarizability elements. To evaluate the currents we consider each U-ring as an effective RLC circuit described by the basic Kirchhoff equation

$$L\frac{\mathrm{d}I_{a,b}}{\mathrm{d}t} + RI_{a,b} + \frac{Q_{a,b}}{C} = U_{a,b} \tag{4}$$

where the subscripts a and b refer to the configuration of Figure 7a,b, respectively, I is the current, Q the corresponding charge ($I = \mathrm{d}Q/\mathrm{d}t$), L the inductance, R the resistance, and C the capacitance of each configuration. The source term, U, is the electromotive force (EMF = $\int \mathbf{E}\cdot\mathrm{d}\mathbf{l}_c + \mu_0\mathbf{S}\cdot\mathrm{d}\mathbf{H}/\mathrm{d}t$; l_c: conductor length, S: loop-current-enclosed area) resulting from both the external and the induced fields. U for the configurations a and b can be written as

$$U_a = -E_y d + E_x 2l\sin\phi - \mu_0 ld\cos\phi\frac{\mathrm{d}H_x}{\mathrm{d}t} - \mu_0 l^2\cos\phi\sin\phi\frac{\mathrm{d}H_y}{\mathrm{d}t} \tag{5}$$

$$U_b = E_x d + E_y 2l\sin\phi + \mu_0 ld\cos\phi\frac{\mathrm{d}H_y}{\mathrm{d}t} - \mu_0 l^2\cos\phi\sin\phi\frac{\mathrm{d}H_x}{\mathrm{d}t} \tag{6}$$

where μ_0 is the vacuum permeability and l, d, ϕ are the geometrical parameters defined in Figure 7.

Note that, for ϕ = 0, for the configuration a the magnetic resonance of the structure can not be excited by the incident fields (E_x, H_y), while for the configuration b both incident electric and magnetic fields are able to excite loop currents in the U-ring, that is, the structure is bianisotropic.[59,60]

Considering harmonic time dependence of the form of $e^{-i\omega t}$, one can calculate the current in Equation (4), the corresponding charge $Q = I/(-i\omega)$ and, through them, the electric and magnetic dipole moments, $\mathbf{p} = Q\mathbf{d}_{cs}$, $\mathbf{m} = I\mathbf{S}$ ($\mathbf{d}_{cs}$ is the charge separation and **S** the area enclosed by loop currents), as a function of the fields, and the polarizabilities as defined by Equation (3). The details of the corresponding calculations are given in the Supporting Information.

For qualitative analysis we can consider the total electric and magnetic dipole moments of our double-ring meta-atom as the sum of the dipole moments of configurations a and b (any coupling between the two perpendicular rings is implicitly taken into account through the modification of induced currents in each ring). Having at hand the total electric and magnetic dipole moments of the unit cell, the electric polarization and the magnetic polarization can be calculated via $\mathbf{P} = \mathbf{p}/V$ and $\mathbf{M} = \mathbf{m}/V$, respectively, where V denotes the volume of the unit cell. (Note that we again ignore here, for simplicity, the coupling between unit cells.)

Then the macroscopic (average) material parameters of our structure, including the chirality, which is crucial for the understanding of its chiral response, can be obtained taking into account the standard constitutive relations $\mathbf{D} = \varepsilon_0\mathbf{E} + \mathbf{P} = \bar{\bar{\varepsilon}}\mathbf{E} + i(\bar{\bar{\kappa}}/c)\mathbf{H}$ and $\mathbf{B} = \mu_0(\mathbf{H} + \mathbf{M}) = \bar{\bar{\mu}}\mathbf{H} - i(\bar{\bar{\kappa}}^T/c)\mathbf{E}$. Applying this procedure (see Supporting Information), the effective permittivity and permeability for the double ring result to be scalar quantities (i.e., diagonal tensors with equal elements; note that for each isolated U-ring both diagonal and off-diagonal permittivity and permeability tensor elements appear). The chirality parameter though, $\bar{\bar{\kappa}}$, has both diagonal and off-diagonal elements, demonstrating the structure bianisotropy. The diagonal elements, which are the ones involved in the cross-polarized transmission[18,68] are given by

$$\kappa_{xx} = \kappa_{yy} = \frac{\omega c\mu_0 l^2 d\cos\phi\sin\phi}{VL[\omega^2 - \omega_0^2 + i\omega(R/L)]} \tag{7}$$

where $\omega_0^2 = 1/LC$ is the resonance frequency of the structure. The off-diagonal elements are given by

$$\kappa_{xy} = -\kappa_{yx} = \frac{\omega c\mu_0 l\cos\phi(2l^2\sin^2\phi + d^2)}{VL[\omega^2 - \omega_0^2 + i\omega(R/L)]} \tag{8}$$

From Equation (7) one can see that the chirality strength is larger the larger the meta-atom "filing ratio" within the unit cell, a result consistent with the observed in Figure 6 dependence of the cross-polarized transmittance and optical activity on the unit cell size. It seems also that the length of the vertical meta-atom arms plays more pronounced role in the chirality than that of the horizontal arms (for that we consider that the inductance L in Equation (7) is proportional to the ring area ($S = ld$ for ϕ = 0). Finally, as is expected, the chirality is generated by the

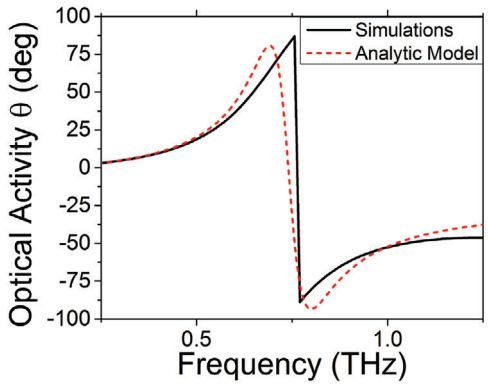

Figure 8. Numerically obtained optical activity, θ, (black line, same as Figure 6c, and fit (dashed red line) using the analytic expression Equation (7). The following parameters were used: $l = d = 96$ μm, $V = 0.12 \times 10^{-12}\text{m}^{-3}$, $L = 1.2 \times 10^{-9}$H, $R = 0.8$~kΩ, $\omega_0 = 4.65 \times 10^{12}\text{s}^{-1}$, $\phi = 30°$, and $D = 130$ μm.

non-zero values of the twist angle ϕ and it is highly affected by ϕ, in consistency also with the results of Figure 6.

Regarding the off-diagonal terms of the chirality tensor, the twist angle ϕ, as is seen by Equation (8), enhances the strength of these terms, that is, it enhances the strength of the bianisotropy. It is not clear though whether this enhancement is the origin of the reduced ellipticity, an effect observed also in ref. [23].

Although the above presented RLC model is mainly qualitative, aiming to demonstrate the dependence of the chiral response on the system parameters, it can also serve to a quantitative analysis. To demonstrate the accuracy with which the RLC model describes our numerical results, we carried out a fit of the optical activity, θ ($\theta = \omega DRe[\kappa_{xx}]/c$), using the analytical Equation (7). In **Figure 8**, we plot the analytic expression for the optical activity as well as the numerical results of Figure 6c (black line). As can be observed in Figure 8, analytic model and numerical simulation are in good agreement. Hence, based on Equation (7) one can determine the optimal conditions/parameters for maximum chiral response of the structure.

5. Conclusion

We have proposed a chiral metamaterial design made of 3D metallic elements for efficient polarization control of electromagnetic waves in a broad frequency range. Particularly, we have demonstrated both numerically and experimentally that our 3D metamaterial, composed of vertical U-shaped resonators of twisted arms, exhibits strong (>45°) and ultrabroadband (relative bandwidth 80%) optical activity with very low ellipticity in the low THz region. The fabrication of the structure was performed through DLW and subsequent electroless silver plating, while the experimental electromagnetic response was demonstrated via THz time domain spectroscopy. Finally, the structures were studied also analytically, though an equivalent RLC circuit model, and the parameters determining its response were identified.

The large, broadband, and pure optical activity of our structure equips it with unique potential for polarization control applications, particularly important in the THz region where there is still a serious lack for efficient optical components. At the same time, our extensive theoretical and numerical study will be instrumental in providing guidance for further expansion and generalization in more complicated systems, where the combination of chirality with other special symmetries or asymmetries may open a new direction in the field of THz photonics.

6. Experimental Section

Photosensitive Material:: The material used for the fabrication of the 3D chiral metamaterial was a zirconium-silicon organic–inorganic hybrid composite doped with metal-binding moieties.[63] It was produced by the addition of methacryloxypropyl trimethoxysilane (MAPTMS) to zirconium propoxide (ZPO, 70% in propanol). 2-(dimethylamino)ethyl methacrylate (DMAEMA) was also added to provide the metal-binding moieties that enabled the selective metallization of the dielectric structures. MAPTMS and DMAEMA were used as the organic photopolymerizable monomers, while ZPO and the alkoxysilane groups of MAPTMS served as the inorganic network forming moieties. 4,4-bis(diethylamino) benzophenone (BIS) was used as a photoinitiator. The photopolymerizable material was synthesized as described in detail in ref. [69]. The samples were prepared by drop-casting onto a 530 μm thick silanized high-resistivity silicon substrate, and the resultant films were dried on a hot plate at 55° for 60 min before the photopolymerization.

Direct Laser Writing by Multiphoton Polymerization:: In DLW, the beam of an ultrafast laser is tightly focused into the volume of a transparent photopolymerizable resin. Polymerization was initiated only within the focal volume element, namely, the voxel, where the intensity was high enough to trigger multi-photon absorption. Scanning the laser beam inside the material, 3D structures could be directly printed, in a layer-by-layer fashion. After the fabrication process was completed, the sample was immersed into appropriate solvents and the unexposed resin was dissolved to reveal the freestanding 3D structure. A droplet of the photosensitive material was placed onto a 530 μm thick silanized high-resistivity silicon substrate for the photopolymerization. A femtosecond fiber laser (FemtoFiber pro NIR, Toptica Photonics AG) emitting at 780 nm with a pulse duration of 150 fs, average output power 500 mW, and a repetition rate of 80 MHz was employed as a light source.[70] A 40× microscope objective lens (Zeiss, Plan Apochromat, N.A. = 0.95) was used to focus the laser beam into the volume of the photosensitive material. A galvanometric scanner-based system (Scanlabs HurryscanII 10, computer-controlled) was used to scan the focused laser beam through the polymeric sample following the predefined metamaterial structure design path. *Z*-axis scanning and larger-scale *x*–*y* movements were possible with the use of a high-precision three-axis linear translation stage (Physik Instrumente). The structures were fabricated in a layer-by-layer fashion starting from the bottom (vertical leg) toward the arms of the structure with the first layer adhering to the surface of the silicon substrate. The scanning speed used was 4000 μm s^{-1}. The power for the fabrication of the structures was measured, before the objective, to be 175 mW. The live-monitoring of the fabrication process was achieved using a CCD camera, with appropriate imaging optics. Finally, an overall 3 × 3 mm^2 metasurface of 24×24 3D chiral meta-atoms array with a periodicity constant of 121.4 μm on the surface of a high resistivity silicon substrate was produced, as is shown in Figure 3.

Metallization:: After the fabrication of the chiral metamaterials array was completed, the metallization process of the sample followed in order for the structures to become conductive and gain optical activity. The metallization process of the 3D chiral metamaterials was based on selective electroless silver plating according to a modified protocol based on ref. [63]. This protocol has been shown to offer conductivity to the microstructures of $\sigma = (5.71 \pm 3.01) \times 10^6$ S m^{-1}.[69] EP is a fairly simple process that did not require any specialized equipment, and the metal deposition could be done without using any electrical potential. In general, it was characterized by the selective reduction of metal ions at the surface of a catalytic substrate immersed into an aqueous solution of metal ions, with continued deposition on the substrate through the catalytic action of the deposit

itself. In detail, EP comprised three main steps: seeding, reduction, and silver plating.

Seeding: The samples were immersed in a 0.05 mol L^{-1} AgNO3 aqueous solution at room temperature for 38 h. This was followed by thorough rinsing with double distilled (d.d.) water and then left to dry at room temperature.

Reduction: An aqueous sodium borohydride (NaBH4) solution 6.6 м was prepared 24 h before the immersion of the samples. The solution was very well mixed and kept uncovered to get rid of trapped air bubbles. The samples were subsequently dipped in the solution for 22 hours to reduce the silver ions and form silver nanoparticles. The samples were washed thoroughly in fresh d.d. water and left to dry.

Silver plating: A 0.2 м AgNO3 aqueous solution was mixed with 5.6% NH3 (28% in water) and 1.9 м glucose ($C_6H_{12}O_6$ > 98%) as a reducing agent, at a volumetric ratio 5:3:8. The samples were immersed in the solution for a few minutes, before the solution turned to dark. In the meanwhile, a fresh solution was prepared to replace the old one. This process was repeated five times.

After the metallization process was completed, the dielectric structure was coated by a thin silver nanoparticles sheet. The thickness of this metal coating on the structures was measured from SEM images, and found to be in the range of 80–130 nm. This means that the core of the structure was still dielectric. The diversity of the thickness parameter resulted from the fact that the metallic coat was not a smooth and bulk layer of silver on the structure surface, but a film of sprinkled metal nanoparticles of varying diameters, that were attached to the structures.

Numerical Calculations:: Numerical calculations were carried out with the commercial software package CST Microwave Studio as well as with the commercial software package COMSOL Multiphysics, employing a finite element solver in the frequency domain. A fine size of tetrahedral spatial mesh was chosen according to the COMSOL physics-controlled mesh. The transmitted and reflected coefficients were simulated for one square unit cell with the periodic boundary conditions on the *x*- and y- sides. The incident waves were excited on the top of the simulation domain by excitation of x- or y-polarized components sweeping the input port 1 or 2, respectively. These ports also measured the reflected x- and y- polarization waves. The detectors at the bottom simulation domain, output port 3 and 4, measured the transmitted *x*- and y- polarization waves. The permittivity of the Silicon substrate was assumed to be constant over the frequency range with $\epsilon = 11.9$ and $\tan(\delta) = 0.02$.

Supporting Information

Supporting Information is available from the Wiley Online Library or from the author.

Acknowledgements

This research work was partly supported by the Hellenic Foundation for Research and Innovation (H.F.R.I.) under the "2nd Call for H.F.R.I. Research Projects to support Faculty members and Researchers" (Project Number: 4542); the European Union, projects In2Sight (FETOPEN-01-2018-2019-2020, GA:964481); FABulous (HORIZON-CL4-2022-TWIN-TRANSITION-01-02, GA:101091644); and the Horizon 2020 RISE Project (CHARTIST, 101007896). Ms Aleka Manousaki provided expert SEM support. Useful communication with Prof. Thomas Koschny is also acknowledged.

Conflict of Interest

The authors declare no conflict of interest.

Author Contributions

I.K., A.T., and M.K. carried out the numerical simulations. I.K. and M.K. developed the theoretical model. M.M. and I.S. fabricated the samples and took the SEM images. A.K., C.D., and C.K. carried out optical characterization experiments. C.S., E.E., S.T., M.F., and M.K. contributed to physical insight, supervised the project, guided manuscript organization, and edited the manuscript. All authors contributed to the preparation of the manuscript.

Data Availability Statement

The data that support the findings of this study are available in the supplementary material of this article.

Keywords

3D chiral metamaterials, direct laser writing, optical activity, THz sources

Received: January 31, 2023
Revised: April 2, 2023
Published online:

[1] J. Lee, M. Tymchenko, C. Argyropoulos, P.-Y. Chen, F. Lu, F. Demmerle, G. Boehm, M.-C. Amann, A. Alú, M. A. Belkin, *Nature* **2014**, *511*, 65.
[2] J. Lee, S. Jung, P.-Y. Chen, F. Lu, F. Demmerle, G. Boehm, M.-C. Amann, A. Alú, M. A. Belkin, *Adv. Opt. Mater.* **2014**, *2*, 1057.
[3] A. C. Tasolamprou, A. D. Koulouklidis, C. Daskalaki, C. P. Mavidis, G. Kenanakis, G. Deligeorgis, Z. Viskadourakis, P. Kuzhir, S. Tzortzakis, M. Kafesaki, E. N. Economou, C. M. Soukoulis, *ACS Photonics* **2019**, *6*, 720.
[4] P. Goulain, A. D. Koulouklidis, J.-M. Manceau, C. Daskalaki, B. Paulillo, K. Maussang, S. Dhillon, J. R. Freeman, L. Li, E. H. Linfield, S. Tzortzakis, R. Colombelli, *ACS Photonics* **2021**, *8*, 1097.
[5] A. D. Koulouklidis, A. C. Tasolamprou, S. Doukas, E. Kyriakou, M. S. Ergoktas, C. Daskalaki, E. N. Economou, C. Kocabas, E. Lidorikis, M. Kafesaki, S. Tzortzakis, *ACS Photonics* **2022**, *9*, 3075.
[6] R. Degl'innocenti, H. Lin, M. Navarro-Cía, *Nanophotonics* **2022**, *11*, 1485.
[7] W. Padilla, A. Taylor, C. Highstrete, M. Lee, R. Averitt, *Phys. Rev. Lett.* **2006**, *96*, 10.
[8] J.-M. Manceau, N.-H. Shen, M. Kafesaki, C. Soukoulis, S. Tzortzakis, *Appl. Phys. Lett.* **2010**, *96*, 2.
[9] N.-H. Shen, M. Massaouti, M. Gokkavas, J.-M. Manceau, E. Ozbay, M. Kafesaki, T. Koschny, S. Tzortzakis, C. M. Soukoulis, *Phys. Rev. Lett.* **2011**, *106*, 3.
[10] C. Stoik, M. Bohn, J. Blackshire, *NDT&E Int.* **2010**, *43*, 106.
[11] T. Nagatsuma, G. Ducournau, C. C. Renaud, *Nat. Photonics* **2016**, *10*, 371.
[12] S. Fan, Y. He, B. S. Ung, E. Pickwell-Macpherson, *J. Phys. D: Appl. Phys.* **2014**, *47*, 37.
[13] A. Shaltout, J. Liu, V. M. Shalaev, A. V. Kildishev, *Nano Lett.* **2014**, *14*, 4426.
[14] L. Cong, W. Cao, Z. Tian, J. Gu, J. Han, W. Zhang, *New J. Phys.* **2012**, *14*, 115013.
[15] Y. Zhao, A. Alú, *Phys. Rev. B: Condens. Matter Mater. Phys.* **2011**, *84*, 20.
[16] L. Cong, W. Cao, X. Zhang, Z. Tian, J. Gu, R. Singh, J. Han, W. Zhang, *Appl. Phys. Lett.* **2013**, *103*, 17.
[17] A. Sarsen, C. Valagiannopoulos, *Phys. Rev. B* **2019**, *99*, 11.
[18] T. Niemi, A. O. Karilainen, S. A. Tretyakov, *IEEE Trans. Antennas Propag.* **2013**, *61*, 3102.
[19] S. C. Meskers, *Mater. Adv.* **2022**, *3*, 2324.
[20] E. Galiffi, P. A. Huidobro, J. Pendry, *Nat. Commun.* **2022**, *13*, 2523.

[21] M. Decker, R. Zhao, C. Soukoulis, S. Linden, M. Wegener, *Opt. Lett.* **2010**, *35*, 1593.
[22] E. Plum, J. Zhou, J. Dong, V. Fedotov, T. Koschny, C. Soukoulis, N. Zheludev, *Phys. Rev. B: Condens. Matter Mater. Phys.* **2009**, *79*, 3.
[23] K. Hannam, D. A. Powell, I. V. Shadrivov, Y. S. Kivshar, *Phys. Rev. B: Condens. Matter Mater. Phys.* **2014**, *89*, 12.
[24] S. S. Oh, O. Hess, *Nano Convergence* **2015**, *2*, 24.
[25] Y. Luo, C. Chi, M. Jiang, R. Li, S. Zu, Y. Li, Z. Fang, *Adv. Opt. Mater.* **2017**, *5*, 16.
[26] H. S. Park, J. Park, J. Son, Y. Kim, H. Cho, J. Shin, W. Jeon, B. Min, *Adv. Opt. Mater.* **2019**, *7*, 19.
[27] C. Caloz, A. Sihvola, *IEEE Antennas Propag. Mag.* **2020**, *62*, 58.
[28] Z. Li, R. Zhao, T. Koschny, M. Kafesaki, K. B. Alici, E. Colak, H. Caglayan, E. Ozbay, C. Soukoulis, *Appl. Phys. Lett.* **2010**, *97*, 8.
[29] C. Menzel, C. Helgert, C. Rockstuhl, E.-B. Kley, A. Tünnermann, T. Pertsch, F. Lederer, *Phys. Rev. Lett.* **2010**, *104*, 25.
[30] M. Mutlu, A. E. Akosman, A. E. Serebryannikov, E. Ozbay, *Phys. Rev. Lett.* **2012**, *108*, 21.
[31] C. Pfeiffer, A. Grbic, *Phys. Rev. Appl.* **2014**, *2*, 4.
[32] I. Katsantonis, S. Droulias, C. M. Soukoulis, E. N. Economou, M. Kafesaki, *Phys. Rev. B* **2020**, *101*, 21.
[33] J. K. Gansel, M. Thiel, M. S. Rill, M. Decker, K. Bade, V. Saile, G. Von Freymann, S. Linden, M. Wegener, *Science* **2009**, *325*, 1513.
[34] B. Wang, J. Zhou, T. Koschny, M. Kafesaki, C. M. Soukoulis, *J. Opt. A: Pure Appl. Opt.* **2009**, *11*, 11.
[35] G. Kenanakis, R. Zhao, N. Katsarakis, M. Kafesaki, C. Soukoulis, E. Economou, *Opt. Express* **2014**, *22*, 12149.
[36] Y. Tang, A. E. Cohen, *Phys. Rev. Lett.* **2010**, *104*, 16.
[37] F. Graf, J. Feis, X. Garcia-Santiago, M. Wegener, C. Rockstuhl, I. Fernandez-Corbaton, *ACS Photonics* **2019**, *6*, 482.
[38] M. Schäferling, D. Dregely, M. Hentschel, H. Giessen, *Phys. Rev. X* **2012**, *2*, 3.
[39] E. Mohammadi, K. Tsakmakidis, A. Askarpour, P. Dehkhoda, A. Tavakoli, H. Altug, *ACS Photonics* **2018**, *5*, 2669.
[40] U. Kilic, M. Hilfiker, A. Ruder, R. Feder, E. Schubert, M. Schubert, C. Argyropoulos, *Adv. Funct. Mater.* **2021**, *31*, 20.
[41] I. Katsantonis, S. Droulias, C. M. Soukoulis, E. N. Economou, T. P. Rakitzis, M. Kafesaki, *Phys. Rev. B* **2022**, *105*, 17.
[42] N. Berova, P. L. Polavarapu, K. Nakanishi, R. W. Woody, *Comprehensive Chiroptical Spectroscopy: Applications in Stereochemical Analysis of Synthetic Compounds, Natural Products, and Biomolecules*, Vol. *2*, Wiley, Hoboken, NJ **2012**.
[43] D. Sofikitis, L. Bougas, G. E. Katsoprinakis, A. K. Spiliotis, B. Loppinet, T. P. Rakitzis, *Nature* **2014**, *514*, 76.
[44] T.-T. Kim, S. Soon Oh, H.-D. Kim, H. Sung Park, O. Hess, B. Min, S. Zhang, *Sci. Adv.* **2017**, *3*, 9.
[45] R. Zhang, B. You, S. Wang, K. Han, X. Shen, W. Wang, *Opt. Express* **2021**, *29*, 24804.
[46] R. Zhao, T. Koschny, C. M. Soukoulis, *Opt. Express* **2010**, *18*, 14553.
[47] A. Khanikaev, N. Arju, Z. Fan, D. Purtseladze, F. Lu, J. Lee, P. Sarriugarte, M. Schnell, R. Hillenbrand, M. Belkin, G. Shvets, *Nat. Commun.* **2016**, *7*, 12045.
[48] S. Golod, A. Gayduk, N. Kurus, V. Kubarev, V. Prinz, *Nanotechnology* **2020**, *31*, 43.
[49] W. Zhang, W. Zhu, E. Chia, Z. Shen, H. Cai, Y. Gu, W. Ser, A. Liu, *Opt. Express* **2014**, *22*, 10446.
[50] K. Song, Z. Su, M. Wang, S. Silva, K. Bhattarai, C. Ding, Y. Liu, C. Luo, X. Zhao, J. Zhou, *Sci. Rep.* **2017**, *7*, 10730.
[51] I. Sakellari, X. Yin, M. L. Nesterov, K. Terzaki, A. Xomalis, M. Farsari, *Adv. Opt. Mater.* **2017**, *5*, 16.
[52] O. Tsilipakos, A. Xomalis, G. Kenanakis, M. Farsari, C. M. Soukoulis, E. N. Economou, M. Kafesaki, *Sci. Rep.* **2020**, *10*, 17653.
[53] G. Kenanakis, A. Xomalis, A. Selimis, M. Vamvakaki, M. Farsari, M. Kafesaki, C. M. Soukoulis, E. N. Economou, *ACS Photonics* **2015**, *2*, 287.
[54] X. Xiong, Z.-H. Xue, C. Meng, S.-C. Jiang, Y.-H. Hu, R.-W. Peng, M. Wang, *Phys. Rev. B: Condens. Matter Mater. Phys.* **2013**, *88*, 11.
[55] H. U. Yang, J. D'Archangel, M. L. Sundheimer, E. Tucker, G. D. Boreman, M. B. Raschke, *Phys. Rev. B: Condens. Matter Mater. Phys.* **2015**, *91*, 23.
[56] N. Laman, D. Grischkowsky, *Appl. Phys. Lett.* **2008**, *93*, 5.
[57] J. Kim, I. Maeng, J. Jung, H. Song, J.-H. Son, K. Kim, J. Lee, C.-H. Kim, G. Chae, M. Jun, Y. Hwang, J. S. Lee, J.-M. Myoung, H. Choi, *Appl. Phys. Lett.* **2013**, *102*, 011109.
[58] Z. Chen, C. Curry, R. Zhang, F. Treffert, N. Stojanovic, S. Toleikis, R. Pan, M. Gauthier, E. Zapolnova, L. Seipp, A. Weinmann, M. Mo, J. Kim, B. Witte, S. Bajt, S. Usenko, R. Soufli, T. Pardini, S. Hau-Riege, C. Burcklen, J. Schein, R. Redmer, Y. Tsui, B. Ofori-Okai, S. Glenzer, *Nat. Commun.* **2021**, *12*, 1638.
[59] R. Marqués, F. Medina, R. Rafii-El-Idrissi, *Phys. Rev. B: Condens. Matter Mater. Phys.* **2002**, *65*, 1444401.
[60] N. Katsarakis, T. Koschny, M. Kafesaki, E. Economou, C. Soukoulis, *Appl. Phys. Lett.* **2004**, *84*, 2943.
[61] A. Ovsianikov, J. Viertl, B. Chichkov, M. Oubaha, B. MacCraith, I. Sakellari, A. Giakoumaki, D. Gray, M. Vamvakaki, M. Farsari, C. Fotakis, *ACS Nano* **2008**, *2*, 2257.
[62] M. Malinauskas, M. Farsari, A. Piskarskas, S. Juodkazis, *Phys. Rep.* **2013**, *533*, 1.
[63] A. Aristov, M. Manousidaki, A. Danilov, K. Terzaki, C. Fotakis, M. Farsari, A. Kabashin, *Sci. Rep.* **2016**, *6*, 25380.
[64] C. Li, C.-C. Chang, Q. Zhou, C. Zhang, H.-T. Chen, *Opt. Express* **2017**, *25*, 25842.
[65] T. Yang, X. Liu, H. Li, C. Wang, J. Sun, J. Zhou, *J. Phys. D: Appl. Phys.* **2020**, *53*, 34.
[66] V. Y. Prinz, E. V. Naumova, S. V. Golod, V. A. Seleznev, A. A. Bocharov, V. V. Kubarev, *Sci. Rep.* **2017**, *7*, 43334.
[67] Q. Zhou, W. Ma, T. Wu, Y. Li, Q. Qiu, J. Duan, J. Li, L. Jiang, W. Zhou, Y. Gao, J. Huang, Z. Huang, *ACS Omega* **2022**, *7*, 36712.
[68] V. S. Asadchy, A. Díaz-Rubio, S. A. Tretyakov, *Nanophotonics* **2018**, *7*, 1069.
[69] N. Vasilantonakis, K. Terzaki, I. Sakellari, V. Purlys, D. Gray, C. M. Soukoulis, M. Vamvakaki, M. Kafesaki, M. Farsari, *Adv. Mater.* **2012**, *24*, 1101.
[70] M. Farsari, M. Vamvakaki, B. N. Chichkov, *J. Optics* **2010**, *12*, 124001.